

A multiwavelength study of the IRAS Deep Survey galaxy sample

III. Spectral classification and dynamical properties

D. Bettoni¹, P. Mazzei¹, and A. della Valle^{1,2}

¹ INAF - Osservatorio Astronomico di Padova, Vicolo dell'Osservatorio, 5 -35122 Padova-ITALY
e-mail: daniela.bettoni@oapd.inaf.it, paola.mazzei@oapd.inaf.it

² INAF - Osservatorio Astronomico di Bologna, Via Ranzani, 1 - 40127 Bologna-ITALY
e-mail: adevalle@gmail.com

ABSTRACT

Context. The infrared deep sample (IDS), in the north ecliptical polar region (NEPR), is the first complete, far-IR selected sample, on which numerous studies of galaxy evolution are based. Such a sample allows direct investigation of the evolution of dusty galaxies up to a redshift of about 0.3, where the global star formation rate is known to evolve very fast. As discussed in previous papers, we performed optical and IR (ISOCAM, 15 μm .) follow-up of its galaxies and exploited our IR observations to correct the 60 μm fluxes for confusional effects and observational biases. In them we found indications of a significant incompleteness of IDS sample below $S(60)\simeq 80\text{mJy}$. We constructed 15 μm and far-IR (60 μm) luminosity functions of a complete sample of 56 ISO/IRAS sources.

Aims. Here we present and analyze the spectral classification of several galaxies in the IDS sample together with rotation curves which allow estimating the lower mass limits of a subsample of objects.

Methods. We measured fluxes and intensity ratios of the emission lines in the visible region of the spectrum ($\lambda 4000 - 9000\text{\AA}$) for 75 galaxy members. Moreover, for some of them (55%), the spectra obtained with the Keck II telescope have sufficient wavelength and spatial resolution to derive their rotation curve.

Results. These galaxies turn out to be disk like systems, with a high fraction ($\sim 50\%$) of interacting systems. The spectroscopic classification of 42 galaxies, using the emission-line ratio diagnostic diagrams, shows that the NEPR sample is predominantly composed of starburst galaxies (71%), while the fraction of AGNs (7%) and LINERs (21%) is small. The dynamical analysis allows us to estimate the lower mass limits of 39 galaxies.

Conclusions. The rest-frame FIR luminosity distribution of these galaxies spans the same range as that of the FIR selected complete sample, i.e. three orders of magnitude, with the same mean value, $\log(L_{FIR})=10.2$. This emphasizes that such galaxies represent FIR properties of the whole sample well. Moreover, their optical properties are typical of the sample itself since 62% of these belong to the 60 μm selected complete sample.

Key words. Galaxies: kinematics and dynamics – Galaxies: fundamental parameters

1. Introduction

One of the most useful tools for studying the physical conditions in galactic nuclei is the analysis of the interstellar medium. The warm ionized gas ($\sim 10^4$ K), for example, is present in the nuclei of nearby galaxies of all morphological types. Detected through optical emission lines, this component of the interstellar medium has served as a diagnostic of the physical conditions in galactic nuclei (Ho et al. , 1993), including their excitation source and chemical abundances, and it allows spectral classification to define the star-forming LINERs and AGN regions. A variety of optical emission-line ratio diagnostics have been presented and employed to determine metallicities, abundances and star formation rates (SFR). In particular, using $[\text{NII}]\lambda 6583/\text{H}\alpha - [\text{OIII}]\lambda 5007/\text{H}\beta$ and $[\text{SII}]\lambda 6717/\text{H}\alpha - [\text{OIII}]\lambda 5007/\text{H}\beta$ ratios diagnostics brings out the separations among the three classes (Baldwin et al. , 1981; Veilleux & Osterbrock , 1987). The separation of extragalactic objects according to their primary excitation mechanisms, together with their photometric and kinematical

properties, leads to a more complete view of their structure and evolution. The spatially extended resolved emission lines provide powerful tracers of the kinematics of a galaxy. These kinematical data are very important because they allow us to derive dynamical masses and to compare them with those obtained from models. In this view, the study of the dynamics of dusty galaxies in the very local universe gives more insight into their evolution.

Far-IR galaxies are dusty objects where a mixture of ongoing AGN activity and star formation play their roles. They are mostly interacting and merging gas-rich spirals (Le Flocc'h et al., 2005) and may represent a link in an evolutionary sequence from spiral galaxies to ellipticals, via mergers. With this connection to early galaxy formation and evolution, the local population can be thought of as a laboratory for studying processes in detail such as SF triggering and starburst vs. AGN interplay. Recent studies suggest many AGNs in IR luminous and massive galaxies (Treister et al , 2010), and Melbourne et al. (2008) have shown that most of dusty galaxies at $z\sim 0.6$ are quite regular disks without evidence of strong interactions.

For this purpose the IRAS Deep Survey (IDS) sample, defined by the Hacking & Houck (1987) co-adding IRAS

Send offprint requests to: D. Bettoni

scans of the north ecliptic polar region and representing more than 20 hours of integration time, is one of the best-suited samples. Mazzei et al. (2001) exploited ISOCAM observations (range 12-18 μm) of 94 IRAS Deep Survey (IDS) fields (Aussel et al., 2000), centered on the nominal positions of IDS sources, to correct the 60 μm fluxes for confusion effects and observational biases. They found indications of a significant incompleteness of the IDS sample below $S(60) \simeq 80 \text{ mJy}$. In della Valle et al. (2006), the first paper of this series (Paper I in the following), we presented spectroscopic and optical observations of candidate identifications of our ISOCAM sources, and the redshift distribution of the 60 μm complete subsample defined by Mazzei et al. (2001) comprising 56 sources. In the second paper, Mazzei et al. (2007) (Paper II in the following), we derived the 60 μm luminosity function (LF) and the poorly known 15 μm LF with the bivariate method of such a sample.

The optical data, together with IR and far-IR (FIR) ones, are very useful for an integral view of the properties of galaxies in our sample. In particular we will derive the spectral energy distribution (SED) extended over several orders of magnitude in wavelength to analyze the evolution of these dusty galaxies over several Gyr in look-back time, i.e., over an interval of time in which the average SFR in the Universe is known to evolve strongly (in prep).

In this paper we give new spectroscopic observations of 75 galaxies and classification of 42 galaxies, thus extending our previous far-IR (FIR) data to the optical, an essential step, in getting a complete view of these galaxy properties. Moreover, dynamical parameters are derived for 41 galaxies in the sample. The plan of the paper is the following. In Sections 2 we summarize our spectroscopy runs, which are fully described in Paper I, and present the more important spectral corrections. In Section 3 we analyze the spectral properties of our sample inside a fixed physical radius of 3 Kpc, to derive their general classification. Section 4 focuses on the analysis of dynamical parameters and the rotation curves available for 41 and 31 of them, respectively. This analysis allowed us to derive mass lower limits for 39 galaxies in the sample. Finally Section 5 gives our conclusions. Here we adopt $\Lambda=0.7$, $\Omega_0=0.3$ and $H_0=70 \text{ km s}^{-1} \text{ Mpc}^{-1}$.

2. Spectroscopic observations and data analysis

A program of optical imaging and spectroscopy was undertaken to observe our sample. We acquired B and R images and low-resolution spectra of all the objects (106) identified in Aussel et al. (2000). Our targets were observed in different runs in the years 2000 – 2003 with telescopes and instruments whose set up is given in Table 1 (see also Table C.1 in Paper I). Sixty-five IRAS fields were observed and spectra of 81 ISOCAM sources taken. In general the slit was oriented along the apparent major axis of the object. In those fields where a double component is visible, as discovered in our previous works (Aussel et al. (2000), and Paper I), the slit was oriented to take the spectra of both galaxies simultaneously. We discovered that ten of our targets (3-04A, 3-10A, 3-44A, 3-49A, 3-57A, 3-65A, 3-78C, 3-83A, 3-85A, 3-89A) were physical pairs of galaxies with the same redshift estimate, and four objects (3-17A, 3-20B, 3-72A, 3-86A) were stars, so the total number of galaxies observed is 87, and out of them 85 have spectra with a

good S/N. In this sample three galaxies (3-13A, 3-57A2, 3-68A) have an absorption line spectra, and six more objects show only a very weak ($S/N \sim 2-3$) $H\alpha$ emission line. For these galaxies we can measure the redshift, but the line is too faint to measure the flux. Finally one object, 3-40B, is a very peculiar case: its Keck spectrum, although very noisy, shows only one emission line that we identified as the $Ly-\alpha$ at $z = 2.954$ (see Fig.1). For this ISOCAM source, we only have upper limits both at 60 μm and at 15 μm (Mazzei et al., 2001). Thus the final sample that we analyze is composed of 75 galaxies.

During each observing night some spectrophotometric and radial velocity standard stars were observed with the same configuration grism/slit of the target objects. All the data were reduced using standard IRAF reduction packages¹ and a detailed description of the reduction is given in Paper I. Spectra were classified according to the presence or absence of various emission lines. Observed emission lines included [O II] 3727, $H\beta$, [O III] 4959-5007, $H\alpha$, [N II] 6548-6583, and [S II] 6717-6731. The measured redshifts are reported in Paper I.

In addition to the measure of the lines intensity, the high resolution of the ESI spectra allowed us to measure the rotation curves for almost all the galaxies observed with Keck II (31 galaxies).

2.1. Starlight subtraction

The optical spectra are contaminated and often dominated by the absorption lines of the stellar component, which affect the strengths of most emission lines of interest. The magnitude of this effect depends on the equivalent widths of the emission and absorption lines, and it is generally large in the nucleus of galaxies. For accurate measurements of their fluxes, we must remove the starlight contribution from our spectra. Generally, there are two strategies for removing starlight and thus obtaining a continuum subtracted, pure emission line spectrum: i) an off-nuclear spectrum (without emission lines) is subtracted from the spectrum of the nucleus, or ii) a template spectrum, free of emission lines, is properly scaled to and subtracted from the spectrum of interest.

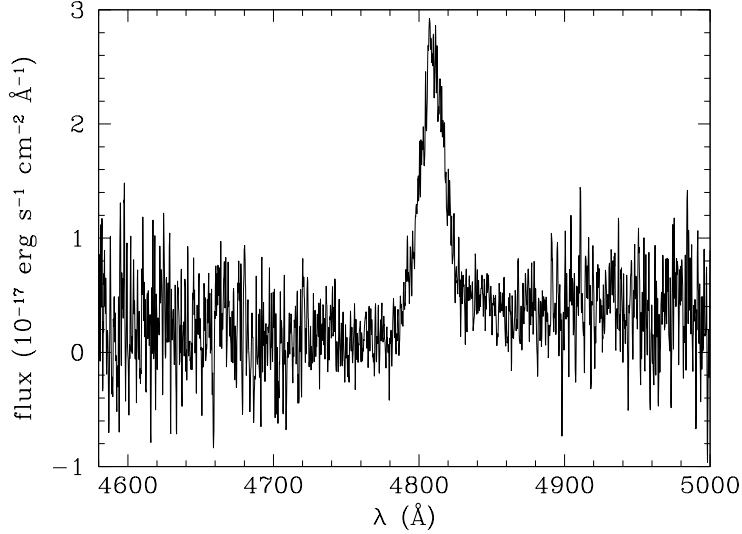
We used the second method, i.e., the technique of Filippenko & Halpern (1984) and Ho et al. (1993). For this purpose, we selected a sample of 57 pure absorption line galaxies from the data of the third data release of the Sloan Digital Sky Survey (SDSS; Abazajian et al. (2005)), whose spectra have very similar characteristics to ours. In particular, to account for the underlying stellar continuum due to the bulge component, template galaxies with different properties such as internal reddening and line strength Lick indices (Mg1, Mg2, Mgb, NaD), have been selected. The line strength indices are in the range typical of an old stellar population, and they include all the values found by Annibali et al. (2007). The internal absorption ranges from zero to $A_v \sim 10 \text{ mag}$ as derived from the $H\alpha/H\beta$ ratio in our sample.

We proceeded with the following steps: i) correct our own spectra and template spectra for Galactic reddening

¹ IRAF is distributed by the National Optical Astronomy Observatory, which is operated by the Association of Universities for Research in Astronomy (AURA) under cooperative agreement with the National Science Foundation.

Table 1. Instrument set-up for every night of observations (see also della Valle et al. 2006)

Telescope	Run	($''$)/pix	Grism grating	Slit ($''$)	λ range(\AA)	Res km/sec
Ekar+AFOSC	28/6/00	0.473	#4	2.1	3360-7740	470
TNG+DOLORES	19/5/01	0.275	LR-R	1.5	4470-10360	300
Keck II+ESI	17/7/01	0.168-0.120	175 lines mm^{-1}	1.0	3900-11000	35
Ekar+AFOSC	25/8/01	0.473	#4, #8	2.1	3360-7740	470
Ekar+AFOSC	12/9/01	0.473	#8	2.1	6250-8050	190
Ekar+AFOSC	9/10/01	0.473	#8	2.1	6250-8050	190
TNG+DOLORES	8/6/02	0.275	LR-R	1.5	4470-10360	300
Keck II+ESI	10/6/02	0.168-0.120	175 lines mm^{-1}	1.0	3900-11000	35
Ekar+AFOSC	17/6/02	0.473	#4	2.1	3360-7740	470
Keck II+ESI	5/9/03	0.168-0.120	175 lines mm^{-1}	1.0	3900-11000	35


Fig. 1. Region of the spectrum of 3-40B source with the Ly α line visible.

using the extinction values of Schlegel et al. (1998), ii) deredshift the spectra to zero, iii) change the resolution of the templates spectra to the resolution of the NEPR ones, iv) subtract the template spectrum from the object spectrum. For each NEPR spectrum, we applied this procedure using all the templates. The best subtraction was chosen using the χ^2 minimization. This method works successfully with the low-resolution spectra of TNG and Ekar telescopes, but it did not work properly with the spectra taken at Keck II. This is due to the large difference between the resolution of the Keck II spectra and that of the template spectra. For this reason we did not subtract the starlight continuum to the Keck II spectra. This implies that fluxes of such emission lines could be underestimated.

In conclusion, for the Ekar and TNG spectra we used the fluxes corrected by the template subtraction. For spectra taken with the Keck II telescope, we used the raw fluxes, corrected only for Galactic extinction. For the Ekar and TNG spectra, we continued our analysis quantifying the error due to the choice of different templates. With this aim for each NEPR spectrum, we compared the flux of H α emission line measured using the different template-subtracted spectra: we found differences from 2% up to 10% in the case of high S/N and low S/N respectively. Figure 2 shows two examples of template-subtraction for high and low S/N spectra.

2.2. Emission line flux measurement

In our observations the slit of the spectrograph was oriented along the apparent major axis of our targets or with a position angle that allows having two galaxies along the slit. For this reason we have to take differential atmospheric refraction (DAR) effects on our measured fluxes into account. To minimize these effects, our observations were made as close as possible to the zenith. In general our targets were observed with air mass ~ 1.4 , and only few cases have higher values. Using the recipes in Filippenko (1982), we derived the angular deviations to correct our fluxes for DAR, taking the air mass and the difference in parallactic angle into account. For the TNG and Ekar observations, we correct the data, were the angular deviation is inside our slit. For eight out of the galaxies observed at Keck II, the conspiracy of both the small slit width ($1''$) and high air mass (≥ 1.8) give an angular deviation that is outside our slit and make DAR correction impossible. In Tables 3 and 4 we mark these galaxies with an asterisk. Moreover, the fluxes were corrected for reddening following the recipes in Rosa-González et al. (2002), adopting the standard Milky Way value for $R=3.1$, and the intrinsic flux ratio of HII region like objects, $F(\text{H}\alpha)/F(\text{H}\beta)$, 2.86. The internal absorption ranges from $A_v \sim 1$ mag to $A_v \sim 14$ mag as derived from the H $\alpha/H\beta$ ratio in our sample. Its average value is $A_v = 6.7 \pm 3.0$ mag with four highly attenuated ob-

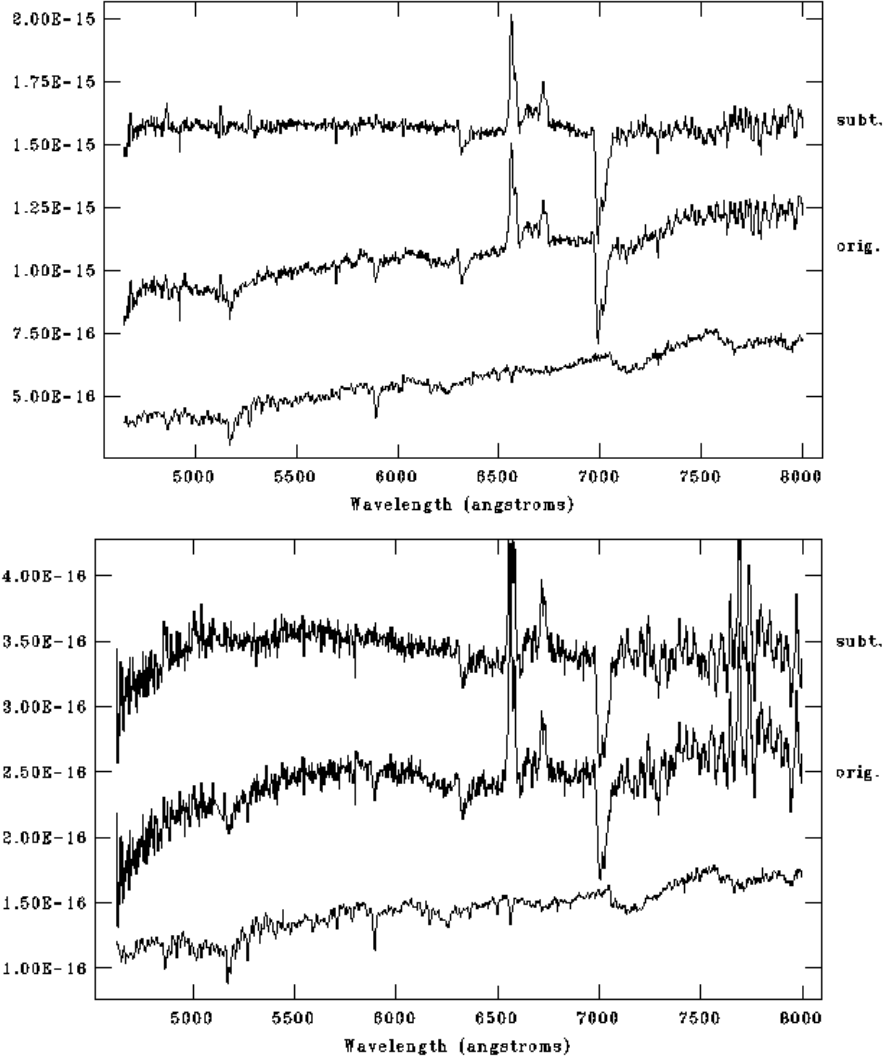


Fig. 2. Top panel: 3-38B, bottom panel: 3-77A. In each panel the bottom plot represents the best fitting template model used to match the stellar component. The middle spectrum is the observed one and the difference at the top. The spectra are scaled by an arbitrary constant.

jects. This is not surprising since our sample is composed of dusty galaxies whose far-IR properties were analyzed in Mazzei et al. (2007). In Table 3 we give the A_v values derived, when available.

This correction, as expected, does not affect the spectral classification.

We measured all the main parameters of the emission lines, i.e. fluxes with their errors (see Tables 3, 4), fitting the emission lines with Gaussian functions. The error estimates of the line fitting are computed by error propagation assuming independent pixel sigmas and no errors in the background. In general in our spectra, the emission lines are also extended along the spatial axis. We decided to perform a measure adding together all the lines in a physical region of 3 Kpc derived using the luminosity distance computed, for each galaxy, according to our cosmological model. This is because, for our more distant objects ($\sim 30\%$ of our sample) the 3 Kpc aperture coincides with the whole optical extension of the galaxy. Thus, with this choice, all the sample is consistently compared.

In this *inner* region, the emission lines can be straightforwardly fitted by a single Gaussian function for almost

all our sample. However there are some peculiar cases, as explained below:

- The emission lines of the spectra of 3-27A and 3-78C2 galaxies showed a double peak. The peaks' separation is 5.4 \AA and 3 \AA respectively, clearly indicating two kinematical components, as discussed in Sect. 4.1. For the lines of these two objects, two Gaussian functions were fitted, and the sum of their area was taken as total flux.
- The spectra of the galaxies 3-44A1, 3-70A, and 3-96A exhibit a broad component in the $H\alpha$ emission line typical of Seyfert I galaxies, which was fitted by adding a second Gaussian function to the fit. The FWHM and the flux of their broad line components are reported in Table 2. Figure 3 shows their spectra and our fits in the $H\alpha$ region.

Note that $[\text{NII}]\lambda 6548$ was not fitted in the high-resolution spectra of 3-16A, 3-65A2, and 3-83A1, because a strong OH emission line of the sky was superimposed on it; however, no flux correction was needed for the $H\alpha$ fluxes of these three

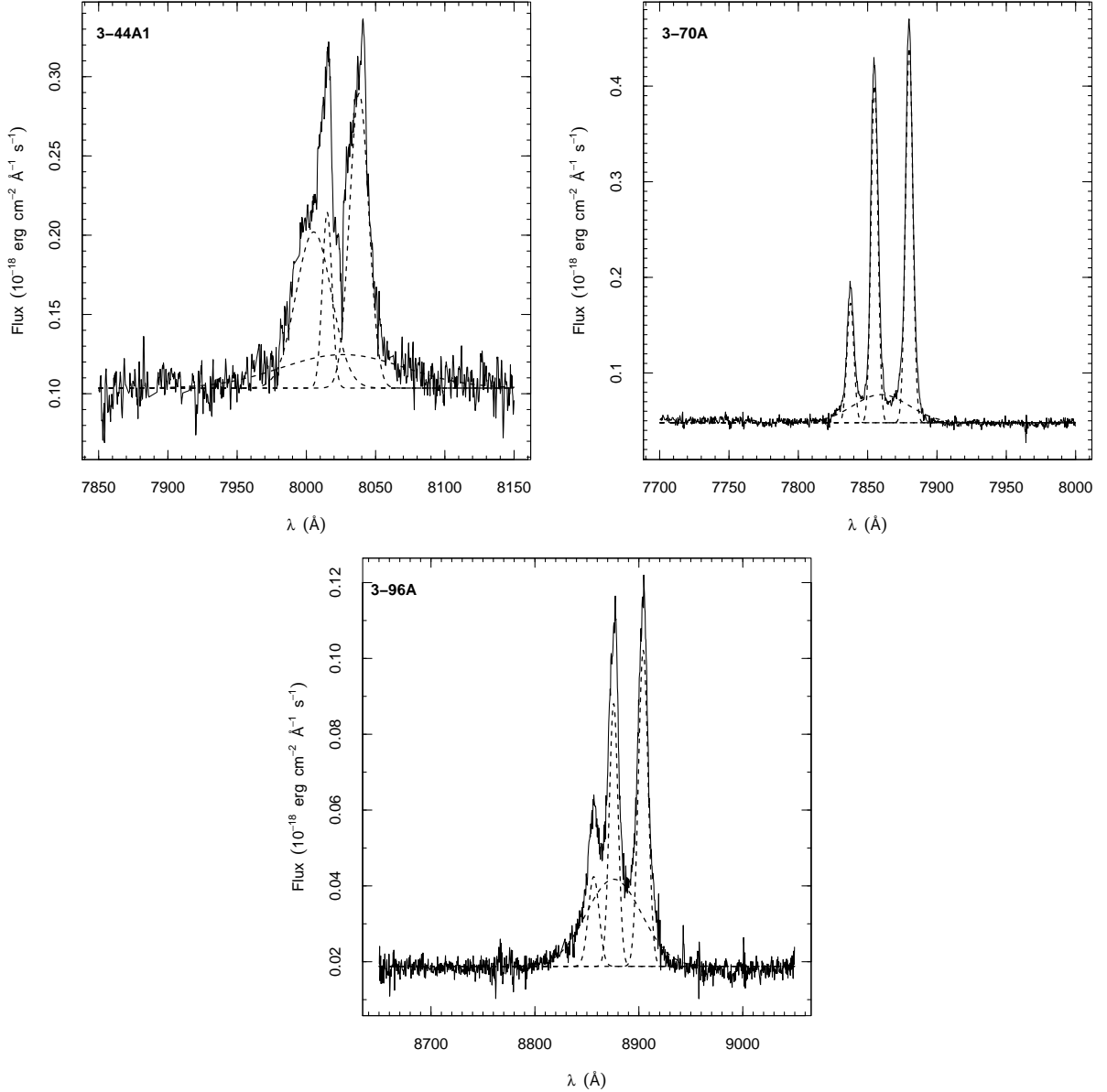


Fig. 3. The H α region for the three AGN (upper left 3-44A1, upper right 3-70A, and bottom 3-96A). The dashed lines show our fits of the broad and narrow components.

objects, since the H α line and [NII] doublet are completely resolved in the Keck II spectra.

When possible (47 spectra), the accuracy of the fit of the H α group was checked by evaluating the strength ratio [NII] λ 6583/[NII] λ 6548 that is expected to be ~ 3 . The values we obtained are in the range $2.5 \div 3.5$.

3. Spectral properties

Figure 4 shows the redshift distribution of all the 85 galaxies described in Paper I. The NEPR supercluster (NEPSC) found by Ashby et al. (1996) (see also Burg et al., 1992) dominates the z -distribution between 0.08 and 0.09. Galaxy members of other expected clusters appear between 0.05 and 0.06, 0.07, and between 0.11 and 0.12. Sixty-one percent of our targets are galaxies with $z < 0.1$, 25% with $0.1 \leq z \leq 0.2$, and 14% galaxies with $z > 0.2$. The mean redshift of the galaxies for which we can measure the rotation

curves (see Section 4) is $\langle z_{\text{rot}} \rangle = 0.141$, and $\sim 50\%$ of these have redshift $z \leq 0.1$.

Tables 3 and 4 present the observed intensities, together with their errors, of the principal emission lines measured inside the physical region of 3 Kpc of our targets. Table 3 includes lines in the red spectral region, between 7000 Å to 5000 Å, and Table 4 those in the blue range, between 5000 Å and 3700 Å.

3.1. Spectral classification

The optical spectral classification as Seyfert (Sy), LINER (L), and star-forming (SF) galaxies, is based on diagnostic diagrams of Veilleux & Osterbrock (1987), a revision of the pioneer work by Baldwin et al. (1981). They exploited four emission-line ratios of the most prominent bright emission lines: [OIII] λ 5007/H β , [NII] λ 6584/H α , [OI] λ 6300/H α and [SII] λ 6716, 31/H α . These line ratios take full advan-

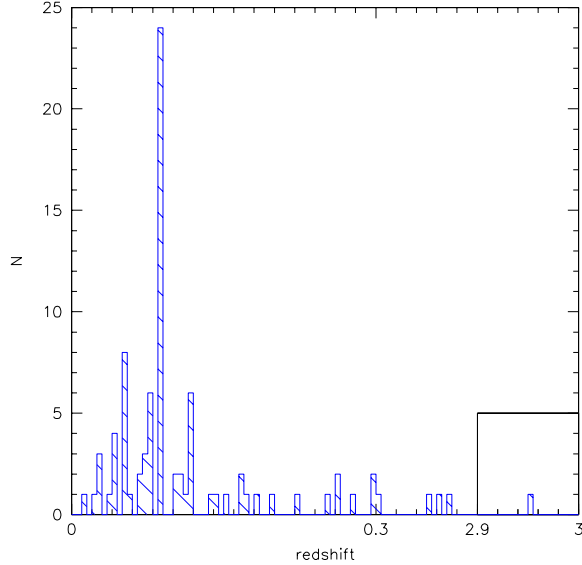


Fig. 4. Redshift distribution of our ISOCAM sources, in 65 IDS/ISOCAM fields. The insert in the lower right corner corresponds the source 3-40B (see text).

Table 2. Broad line data for 3-44A1, 3-70A, and 3-96A

Galaxy name	FWHM km s^{-1}	Flux $10^{-18} \text{erg s}^{-1} \text{cm}^{-2} \text{\AA}^{-1}$
3-44A1	3700	3.712 ± 0.896
3-70A	2260	1.416 ± 0.083
3-96A	2870	1.740 ± 0.050

tage of the physical distinctions between the various types of objects and minimize the effects of reddening correction and calibration errors. Diagnostic diagrams have been used ever since as a standard to identify narrow-line active galaxy nuclei (AGN, or Sy). Kewley et al. (2001) (see also Groves & Kewley (2008) and references therein) build up a detailed starburst model with large ranges of metallicity and ionization parameter, finding upper limits to separate starburst from AGN on such diagrams. Star-forming (SF) galaxies fall onto the lower left-hand region of these plots, narrow-line Sy are located in the upper right, and Ls in the lower right-hand zone. Thus, to separate the different types of galaxies (Sy, L, SF galaxies) we used the theoretical boundaries of Kewley et al. (2001).

Figure 5 shows the position of our galaxies on these diagrams, including galaxies in the $60 \mu\text{m}$ complete sample ($S_{60} \geq 80 \text{mJy}$) of Mazzei et al. (2001). The data refer to the fluxes measured in the inner physical 3 Kpc region of the galaxies. Three galaxies, 3-44A1, 3-70A, and 3-96A, show the $\text{H}\alpha$ with a broad line component (Fig. 3), and we classified them as Sy 1. In Fig. 5 they are residing in the AGN region and will be discussed further below. Table 2 presents the FWHM and fluxes of their broad line $\text{H}\alpha$ emission, and Tables 3 and 4 the fluxes of their narrow line components used in the spectral classification.

In our sample there are 25 objects (33%) with all the four available diagnostic ratios (see Fig. 5). However, it is possible to address a spectral classification for other 17 galaxies using only two diagnostic diagrams, so we classify a total of 42 galaxies (56% of the observed ones).

After analyzing the diagnostic diagrams (Fig. 5) following Kewley et al. (2006) and Groves & Kewley (2008), all the galaxies below the pure SF line defined by Kauffmann et al. (2003) are SF. We found that 16 out of 25 galaxies with all four ratios available, turn out to be SF galaxies.

To classify all the remaining galaxies we used the theoretical one sigma boundaries between the regions occupied by LINERS (L) and AGN in these diagnostic plots, as in Kewley et al. (2006). We note that two galaxies are certainly inside the region that defines the Ls, and seven more galaxies are in the region defined by the one sigma boundaries as Ls. The emission lines in the spectra of these seven galaxies do not have a broad line component. This point further favors their classification as Ls. Following all these criteria, the three AGN galaxies discussed above appear in the upper right-hand region of our diagnostic plots as expected.

A tentative spectroscopic classification of 3-84A was made by Ashby et al. (1992) obtaining an ambiguous result: they found that this galaxy has $[\text{NII}]\lambda 6583$ emission indicative of a star-burst, ambiguous $[\text{SII}]$ emission, and $[\text{OI}]\lambda 6300$ emission characteristic of an AGN. Following previous discussion we classify this galaxy as an L (see Table 5). Finally, we found

- 30 SF (71% and 40% of the classified and observed galaxies respectively),
- 3 Sy 1 (7% and 4%)

– 9 L (21% and 12%)

Table 5 summarizes our spectral classification. Figure 6 shows the distribution of the rest-frame FIR luminosity, L_{FIR} from 42.5 to 122.5 μm , where

$$L_{FIR} = 4\pi D^2(FIR) \quad (1)$$

$$FIR = 1.26 \times 10^{-14}(2.58f_{60} + f_{100}) W/m^2, \quad (2)$$

and f_{60} and f_{100} are in Jy (Helou et al. , 1988), of the 35 ISO sources corresponding to the 42 galaxies in Table 5. In particular, in Table 5, 30 SF galaxies correspond to 26 ISO/IRAS sources, and three of these, 3-78C, 3-79C, and 3-92A, have no FIR fluxes (Mazzei et al. , 2001), so there are 23 ISO/IRAS sources classified as SF types in the right-hand panel of Fig. 6. In this figure, as in the following ones, K-corrections were derived from evolutionary population synthesis models taking dust effects into account (Mazzei et al. , 1995), and luminosities were in units of solar bolometric luminosity, $L=3.83 \times 10^{33}$ erg/s. Moreover, upper limits to flux densities were accounted for by exploiting the Kaplan-Meier (KM) estimator (Kaplan & Meier , 1958), as in Paper II. Calculations were carried out using the ASURV v 1.2 package (Isobe & Feigelson , 1990), which implements methods presented in Feigelson & Nelson (1985) and in Isobe et al. (1986). The KM estimator is a nonparametric, maximum-likelihood-type estimator of the true distribution function (i.e., with all quantities properly measured, and no upper limits). The survivor function, giving the estimated proportion of objects with upper limits falling in each bin, does not produce, in general, integer numbers, but is normalized to the total number. This is why noninteger numbers of objects appear in the histograms of our figures.

The average value of the LFIR distribution, which accounts for 18 upper limits, is $\log(LFIR)=10.3$ (Fig. 6, left panel), very close to the average value of the FIR selected complete sample of Mazzei et al. (2007). Liner galaxies show the same average LFIR whereas, by accounting only for SF types, this slows down slightly, 9.9 (Fig. 6, right panel).

4. The rotation curves

The spectra obtained with the Keck II telescope have both wavelength and spatial resolution high enough to allow us to measure the galaxy rotation curves (RC). Only three galaxies do not show emission lines and for this reason we have such data for 31 out of the thirty-four galaxies observed with this instrument (41% of the whole sample of observed galaxies). To measure the RCs, a Gaussian function was fitted on the $H\alpha$ emission lines with $S/N \geq 2$. In some cases more than one component was detected, either because of the presence of two decoupled kinematic components as in 3-26B and 3-27A or because of interacting regions of two galaxies (3-78C2).

Since the main goal of our spectroscopic observations was to measure the redshifts of the NEPR galaxies, the slit position of the spectrograph was not always placed along the galaxy major axis: for example, some objects were observed simultaneously in the same exposure (see Section 2). The slit orientations therefore, have heterogeneous misalignment respect to the real major axes of the galaxies:

for nine out of them the misalignment is less than ten degrees, and the slit was oriented along an oblique axis for the remaining 22 galaxies. This misalignment angle, δ , has been measured for all the Keck II spectra, and it is reported in Table 6. The redshift distribution of 31 galaxies for which we measured the RCs is shown in the left-hand panel of Fig.7. The mean redshift of the distribution is $\langle z_{\text{rot}} \rangle = 0.141$, the nearest galaxy is 3-29A with $z = 0.0408$, and the most distant one is 3-53A1 with $z = 0.3723$. Fifteen galaxies have a redshift $z \leq 0.1$. Two galaxies (3-44A2 and 3-53A1) have $z > 0.3$. The observed RCs have been modeled with the normalized \arctan rotation curve function:

$$v(r) = v_0 + \frac{2}{\pi} v_* \arctan(R) \quad (3)$$

where $R = (r - r_0)/r_t$, and v_0 is the systemic velocity of the nucleus, r_0 the spatial center of the galaxy, v_* the asymptotic velocity, and r_t the transition between the rising and flat parts of the rotation curve (Courteau , 1997). In Figs. 9 and 10, the best fit (Eq. 3, continuous line) is shown.

To enlarge the sample of kinematical data in Table 6, we included the results from some low-resolution spectra obtained with the TNG telescope. These spectra do not allow the measure of the RCs; nevertheless, since the spectra of the ten galaxies observed with this telescope (3-23A, 3-31A, 3-38A, 3-47A, 3-59A, 3-61A, 3-81A, 3-81B, 3-88A1, 3-93A) are spatially resolved, we succeeded in measuring at least the Δv , i.e., the velocity difference between the core and the outer regions. The redshift distribution of these galaxies is shown in the left-hand panel of Fig. 7. The mean redshift of the distribution is $\langle z_{\text{rot}} \rangle = 0.063$, the nearest galaxy is 3-31A with $z = 0.0267$, and the most distant is 3-38A with $z = 0.0883$. Usually, we extracted regions around the core of 1.4'' with the exception of 3-59A (1''), 3-88A1 (1''), and 3-93A (2.24''). Then, we extracted spectra of two regions in the outer part of the galaxies. For each of these spectra, the position of the blending group of $H\alpha$ and [NII] emission lines was measured. For four galaxies (3-23A, 3-31A, 3-59A, 3-61A), these three emission lines were deblended, while in the remaining ones only the positions of $H\alpha$ and [NII] were measured. Since [NII] is much weaker than $H\alpha$, we considered its contribution negligible. Finally, the velocity difference, Δv , between the velocity of the nucleus and in the outer region was calculated.

4.1. Notes concerning peculiar RCs

Most of the thirty-one RCs in Figs. 9 and 10 are very regular, which is typical of disk galaxies; however, some show peculiar motions, very disturbed rotation patterns, and in few cases, kinematic decoupled regions that were excluded from the fit of RC. In the following we summarize the puzzling features.

3-10A: this ISO/IRAS source is composed of two galaxies, A1 and A2, at both the same redshift (della Valle et al. , 2006). Their disturbed RCs show these are interacting/merging galaxies.

3-12A: its RC extends beyond 8 Kpc, but only the region of rigid rotation is visible. No imaging is available to confirm this point.

3-20: also in this case, the RC extends more than 9 Kpc, showing only the rigid rotation zone; there is no imaging available for this source either.

3-26B: this is a edge-on spiral galaxy. Its RC shows a double component in the northern region, towards the companion galaxy 3-26A. In the GALEX archival images, a bridge connecting the two galaxies appears in the same region where the RC curve shows the double component; the plateau of its RC is hinted at because the slit of the spectrograph, placed along the major axis, is smaller than the apparent dimension of such a galaxy.

3-27A: two inner velocity components separated by more than 200 km/s arise in the RC of this galaxy. They correspond to the opposite sides of a fast rotating ring decoupled from the disk motion.

3-30A: the west side of its RC, with the photometric center 2.2 arcsec far from the dynamical center, shows perturbed behavior. This pattern may be a signature of an outburst or of some type of interaction; however, no imaging is available to explain the peculiarity of such an RC.

3-37A: this galaxy corresponds to PGC3086419 (HYPERLEDA catalog), but also in this case no imaging deep enough is available to solve the puzzle of its RC.

3-40A: even if this galaxy corresponds to PGC2699424 (HYPERLEDA) and to 2MASX J17562643+6723549, the resolution of available images cannot explain the very perturbed RC of this galaxy that could be the signature of a fast rotating inner bar.

3-53A: this is the highest redshift (0.37) galaxy belonging to the 60 μm complete ($S_{60} > 80 \text{ mJy}$) sample (Mazzei et al. , 2001), and its RC only refers to the slowly rotating inner region.

3-65A: this ISO/IRAS source is composed by a pair of galaxies, A1 and A2 (della Valle et al. , 2006); the north-west distortion of RC of A1 galaxy cloud be due to the interaction with its companion galaxy, A2; however, our imaging do not confirm tidal distortions.

3-66A: there is an anomaly in the western region of its RC, which can be explained, looking at the DSS image (the only available so far), by an outburst visible in the north-west side of this galaxy.

3-69A: the anomaly arising in the north-east region of its RC may be due to a companion galaxy. No imaging with enough resolution is available to elucidate this point.

3-76A: in the south-east region of its RC a perturbation arises that, considering the 2MASS image (2MASXJ18042694+6720481), may be due to a faint object near the galaxy.

3-78C2: there is a double component in the RC of this galaxy that may be due to interaction; however, its companion galaxy, 3-78C1, shows no signs of tidal interaction.

We derived the spectral classification of 28 out of the 31 galaxies with RCs. For three objects, namely 3-40, 3-45, and 3-76, no [OIII] λ 5007 is detected. Twenty-three galaxies (77%) are classified as SF, four (13%) as L, and one as Sy. We note that Ls and Sy show an almost regular RC, while the SF galaxies show the distortions and peculiarities typical of interactions.

4.2. Mass estimates

We defined v_{opt} as the velocity measured at the maximum spatial extent in arcsec (r_{opt}) of either the approaching or the receding side of the galaxy spectra. No rotation curve shows the flat region of the curve clearly.

Velocities are corrected for projection on the sky, cosmological stretch, and misalignment angle. Therefore, the corrected v_c is there

$$v_c = \frac{v}{(1+z) \sin i \cos \delta} \quad (4)$$

where the inclination along the line of sight, i , was estimated using the observed axis ratio derived from the CCD images when available (see Paper I), and the POSS images for the others; an intrinsic flattening, q_0 , of 0.20 for all the galaxies is assumed. We use

$$\cos^2 i = \frac{q^2 - q_0^2}{1 - q_0^2} \quad (5)$$

where the adopted i for each galaxy is given in Table 6.

The misalignment angle is a critical parameter for our measurements, because several spectra were observed far from the major axis. Following the simulation of Giovannelli et al. (1997), errors due to this correction are negligible for position angle offsets less than 15°. For seventeen galaxies this condition is verified. For two, 3-65A2, and 3-70A, this correction is instead not applicable, because they were observed very close to the minor axis. For other two galaxies, 3-10A2, and 3-81A the mass estimates is affected by this correction (see Table 6).

Using the derived velocity v_c , we estimated the mass inside the last observed point of thirty-nine galaxies, i.e., a lower limit to the mass of our galaxies, with the relation by van der Bosch (2002):

$$M_{vir} = 2.54 \cdot 10^{10} M_{\odot} \left(\frac{r_d}{\text{Kpc}} \right) \left(\frac{v_c}{100 \text{ kms}^{-1}} \right)^2 \quad (6)$$

where r_d is the virial radius. We used the radius R_{opt} in Kpc as defined above as r_d . These estimates are summarized in Table 6.

The right-hand panel of Figure 7 shows the mass distribution of galaxies in Table 6 and Fig. 8. The left-hand panel shows the same, accounting for KM estimator assuming lower mass limits when the RCs are less extended than 8 Kpc, and for all the Δv estimates. The mass distribution spans more than three orders of magnitudes. For eleven galaxies the masses are derived in the nuclear region, i.e., ($R_{opt} < 5 \text{ Kpc}$). The mean value of the distribution accounting for only RCs, i.e. 31 galaxies, is $3.66 \cdot 10^{11} M_{\odot}$, and $4.93 \cdot 10^{11} M_{\odot}$ including all the galaxies. We point out that the high velocity, v_{opt} , measured for the 3-61A galaxy (see Table 8) may be due to dynamical perturbations induced by interaction with a dwarf compact companion $\simeq 11.5$ arcsec north of this barred galaxy, as derived by combining the imaging and spectrum of this ISO/IRAS source. By removing this galaxy from the mass sample, the last bin in Fig. 7 (right panel) and in Fig. 8 (left panel) disappears, so that the mean value of the whole mass distribution is $3.68 \cdot 10^{11} M_{\odot}$, the same as derived from galaxies with RC measured.

We note that the 67% of these galaxies belongs to the 60 μm selected, complete sample defined by Mazzei et al. (2001). The right-hand panel of Fig. 8 shows the rest-frame FIR luminosity distribution of 32 ISO/IRAS sources corresponding to galaxies in Table 6. Four galaxies i.e., 3-10A2, 3-78C2, 3-83A2, and 3-83A2 are multiple optical counterparts of the same ISO/IRAS source (della Valle et al. ,

2006); moreover, no FIR fluxes are available for 3-38A and 3-78C and 3-81B which result as confused sources in Mazzei et al. (2001). Mazzei et al. (2007) show that the FIR luminosity of the IDS/ISOCAM sample extends over three orders of magnitude (see their Fig. 9, left panel), as in Fig. 8, and with the same mean value, $\log(L_{FIR})=10.2$. This is almost the same as for the Revised IRAS $60\mu\text{m}$ Bright Galaxy Sample (Sanders et al. , 2003) and for a normal spiral galaxy, like the Milky Way (Mazzei et al. , 1992). The ultraluminous infrared galaxy 3-53A emits the maximum FIR luminosity of the sample, nearly 100 times higher than the mean value.

5. Conclusions

The spectral classification of 42 galaxies, with the emission line ratio diagnostic diagrams, shows that the NEPR sample is predominantly composed of SF, starburst galaxies (71%), while the fraction of LINERs (21%) and AGNs (7%) is smaller. Three new Sy 1 galaxies were identified, 3-44A1, 3-70A, and 3-96A. The rest-frame FIR luminosity distribution of galaxies with spectral classification spans the same range as the FIR-selected complete sample analyzed by Mazzei et al. (2007), i.e. three orders of magnitude, with the same mean value, $\log(L_{FIR})=10.2$. This emphasizes that such galaxies represent FIR properties of the whole sample well. Moreover, their optical properties are typical of the sample itself since 62% of these belong to the $60\mu\text{m}$ selected complete sample of galaxies defined by Mazzei et al. (2001) (see della Valle et al. (2006)).

Using the rotation curves and spatially resolved, low-resolution spectra, we are able to derive dynamical parameters of 41 galaxies and mass estimates, inside the last point viewed, of 39 galaxies in the sample. We point out that the 67% of them belong to the $60\mu\text{m}$ complete sample cited above. Moreover, also in this case, their rest-frame FIR luminosity distribution extends over the same range and has the same mean value as expected for the complete sample. The mass distribution extends over three orders of magnitude with a mean value of $\langle M \rangle = 3.66 \cdot 10^{11} M_{\odot}$, slightly more than the Milky Way, where Wong et al. (2004) find a mass of $1.3 \cdot 10^{11} M_{\odot}$ within 12 Kpc of the Galactic center.

Paper I concluded that two or more galaxies with very close redshifts may contribute to the ISOCAM/IRAS flux in at least seven cases (3-04A, 3-10A, 3-57A, 3-65A, 3-78C, 3-83A, 3-89A). Dynamical perturbations of the rotation curves discussed here prove that 3-10A and 3-65A are interacting/merger systems. Interactions also involve the 3-78C2 galaxy, and disturbed patterns appear in the rotation curve of 3-83A1; however, 3-89A1 and 3-89A2 galaxies show unperturbed rotation curves.

We find several systems with previously unsuspected decoupled velocity components, 3-26B, 3-27A, 3-37A, and 3-40A. Moreover peculiar motions arise in the rotation curves of 3-26A, 3-30A, 3-66A, 3-69A, 3-70AA, 3-71A, and 3-76A. Thus, 48% of the rotation curves have disturbed morphologies and most part of these are SF galaxies. This emphasizes the role of interactions in triggering starbursts and, in particular, FIR emission in our sample of dusty galaxies.

Acknowledgements. We thank the anonymous referee whose comments greatly improved the paper. Some of the data presented herein were obtained at the W.M. Keck Observatory, which is operated as a scientific partnership among the California Institute of Technology, the University of California, and the National Aeronautics and Space

Administration. The Observatory was made possible by the generous financial support of the W.M. Keck Foundation.

References

- Abazajian, K. et al. 2005, *AJ*, 129, 1755
 Annibali, F., Bressan, A., Rampazzo, R., Zeilinger, W. W., & Danese, L. 2007, *A&A*, 463, 455
 Aussel, H., Coia, D., Mazzei, P. et al. 2000, *A&AS*, 141, 257
 Ashby, M., Houck, J., Hacking, P., 1992, *AJ*, 104, 980
 Ashby, M., Hacking, P., Houck, J., et al. 1996, *ApJ*, 456, 428
 Baldwin, J. A., Phillips, M. M., & Terlevich, R., 1981, *PASP*, 93, 5
 Burg, R., Giacconi, R., Huchra, J. et al. 1992, *A&A* 259, L9
 Courteau, S. 1997, *AJ*, 114, 2402
 della Valle A., Mazzei, P., Bettoni, D. et al. 2006, *A&A* 454, 453
 Feigelson, E., Nelson, P. 1985, *ApJ*, 293, 192
 Filippenko, A.V. 1982, *PASP*, 94, 715
 Filippenko, A. V & Halpern, J.P., 1984, *ApJ*, 285, 458
 Hacking, P., Houck, I.R. 1987, *ApJS*, 63, 311
 Hacking, P., et al. 1989, *ApJ*, 339, 12
 Giovannelli, R., Haynes, M. P., Herter, T., Vogt, N. P., da Costa, L. N., Freudling, W., Salzer, J. J. and Wegner, G. 1997, *AJ*, 113, 53.
 Groves, B., Kewley, L. 2008, *APS Conf.S.* 390, 293
 Helou, G., Khan, I., Malek, L., & Boehmer, L. 1988, *ApJS*, 68, 151.
 Ho, L. C., Filippenko, A. V. & Sargent, W. L. W., 1993, *ApJ*, 417, 63
 Isobe, T., Feigelson, E., Nelson, P. 1986, *ApJ*, 306, 490
 Isobe, T. Feigelson, E. 1990, *BAAS*, 22, 917
 Kauffmann, G., et al. 2003, *MNRAS*, 346, 1055
 Kaplan, E., Meier, P. 1958, *J. Am. Stat. Ass.* 53, p. 457
 Kennicutt, R.C.jr. 1998, *ARA&A*, 36 189
 Kewley, L. J., Heisler, C. A., Dopita, M. A. & Lumsden, S. 2001, *ApJS* 132, 37
 Kewley, L. J., Groves, Kauffmann, G., Heckman, T. 2006, *MNRAS* 372, 961
 Le Floch, E., Papovich, C., Dole, H., et al. 2005, *ApJ*, 632, 169
 Mazzei, P., de Zotti, G., Xu, C. 1992, *A&A*, 256, 45
 Mazzei, P., Curir, A., Bonoli, C. 1995, *AJ*, 422, 81
 Mazzei P., Aussel, H., Xu, C. et al. 2001, *New Astr.* 6, 265
 Mazzei, P., della Valle, A. & Bettoni, D., 2007 *A&A*, 462, 21
 Melbourne, J., Ammons, M., Wright, S. A., et al. 2008, *AJ*, 135, 1207
 Rosa-González, D., Terlevich, E., & Terlevich, R. 2002, *MNRAS*, 332, 283
 Sanders, D.B., Mazzarella, J.K, Kim, D., et al. 2003, *AJ*, 126, 1607
 Schlegel, D. J., Finkbeiner, D. P., and Davis, M., 1998, *Apj*, 500, 525
 Treister, E., Urry, C. M., Schawinski, Ke., Cardamone, C. N., Sanders, D. B., *ApJ* 722, L238
 van der Bosch, 2002, *MNRAS*, 332, 456
 Veilleux, S. and Osterbrock, D. E., 1987, *ApJS*, 63, 295
 Wong, O. I., Drinkwater, M. J., Jones, J. B., Gregg, M. D., & Freeman, K. C., 2004, *Dark Matter in Galaxies*, 220, 213

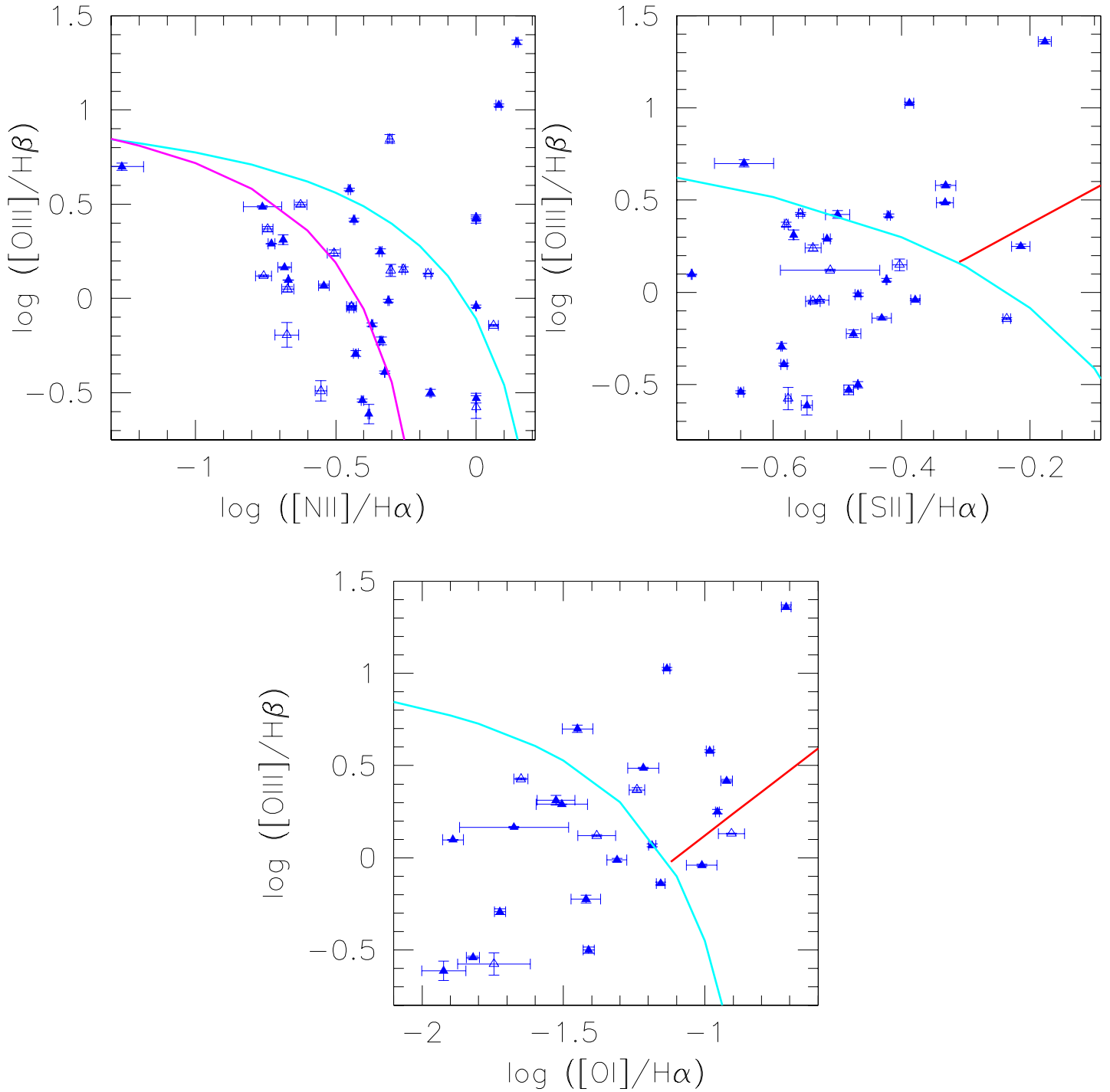


Fig. 5. Emission line diagnostic diagrams. Galaxies belonging to the $60\mu\text{m}$ complete sample of Mazzei et al. (2001) are represented with filled triangles; light (cyan) curves in all the three panels show the extreme starburst definition of Kewley et al. (2001); bold curve (magenta) shows the pure SF limit of Kauffmann et al. (2003); and red lines the LINER/AGN divisions from Kewley et al. (2001) and Kewley et al. (2006). Upper panels: $\log [\text{OIII}] \lambda 5007/\text{H}\beta$ versus $\log [\text{NII}] \lambda 6583/\text{H}\alpha$ and $\log [\text{OIII}] \lambda 5007/\text{H}\beta$ versus $\log [\text{SII}] \lambda 6716, 6731/\text{H}\alpha$. Lower panel: $\log [\text{OIII}] \lambda 5007/\text{H}\beta$ versus $\log [\text{OI}] \lambda 6300/\text{H}\alpha$.

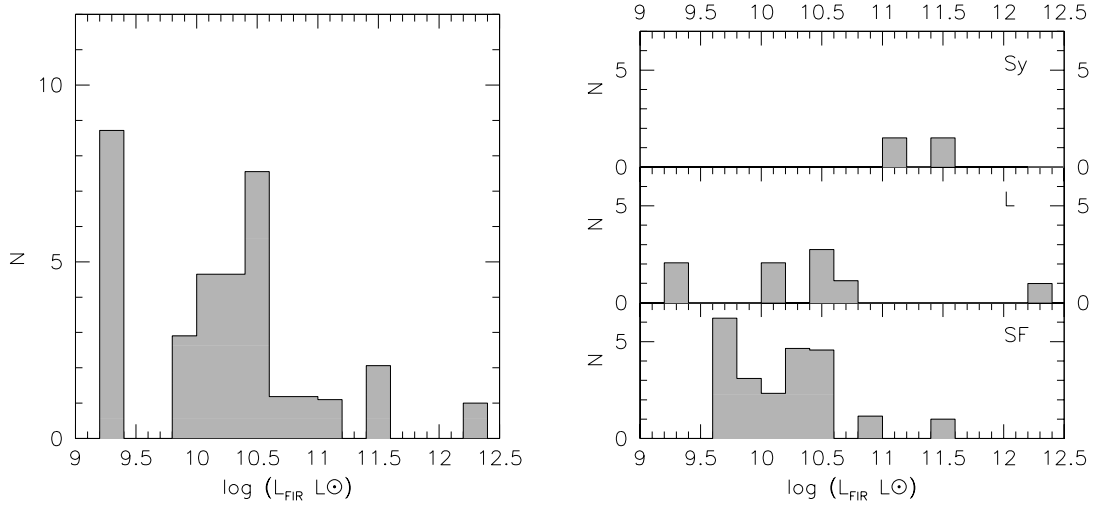


Fig. 6. *Left:* The rest-frame FIR luminosity distribution of 35 ISO/IRAS sources included in this study. Far-IR data (Mazzei et al. , 2001) account for KM estimator (see text). *Right:* As in the left panel accounting for spectral classification here derived (Table 5).

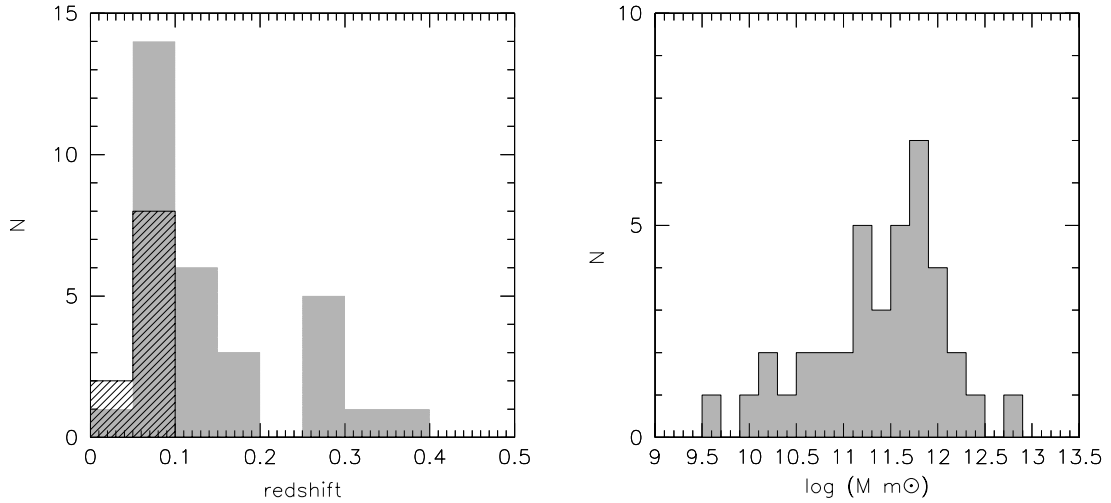


Fig. 7. *Left:* Redshift distribution of 41 galaxies in Table 6: gray histogram is for 31 galaxies with rotation curves, dashed histogram shows the remaining galaxies; the bin size is $\Delta z = 0.05$. *Right:* Mass distribution of 39 galaxies in the same Table (see text); the bin size is 0.2.

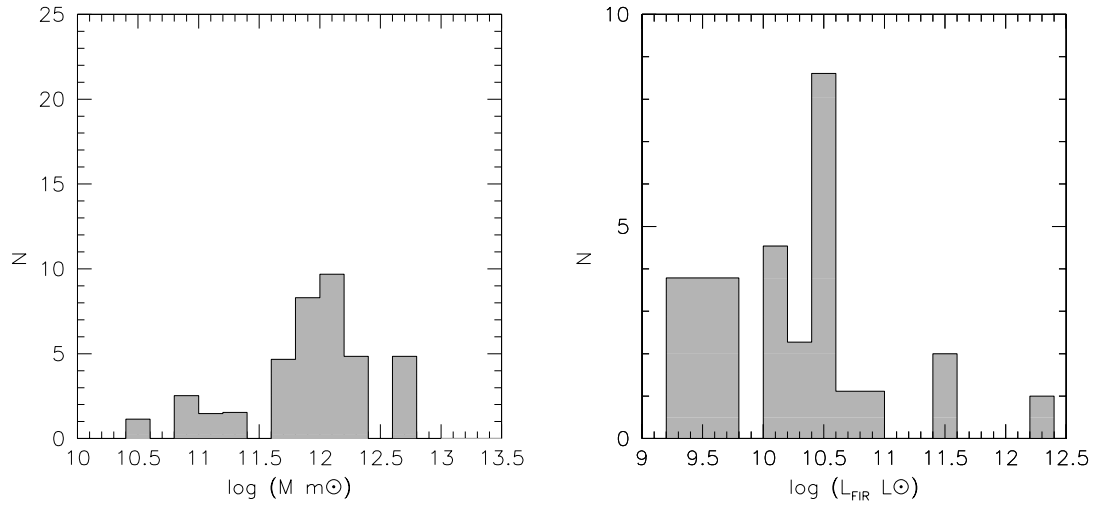


Fig. 8. Left: The same as in Fig. 7 but accounting for KM estimator. Right: The rest-frame FIR luminosity distribution for 32 galaxies with mass estimates exploiting KM estimator to take upper limits to FIR fluxes into account (Mazzei et al. , 2001).

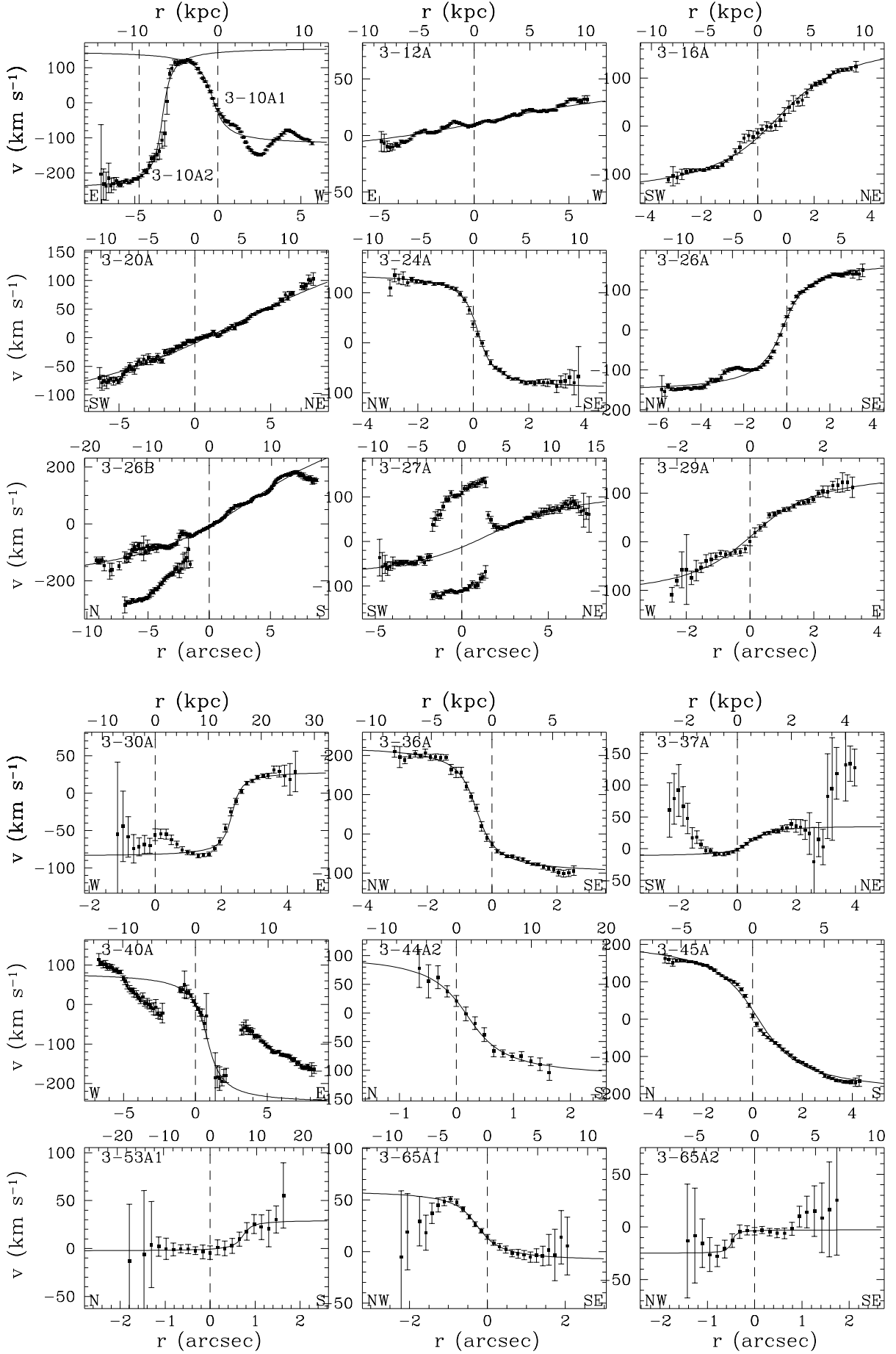


Fig. 9. The observed rotation curves for the galaxies in our sample (at a mean $z \sim 0.1$). The solid line shows the fit with equation (3).

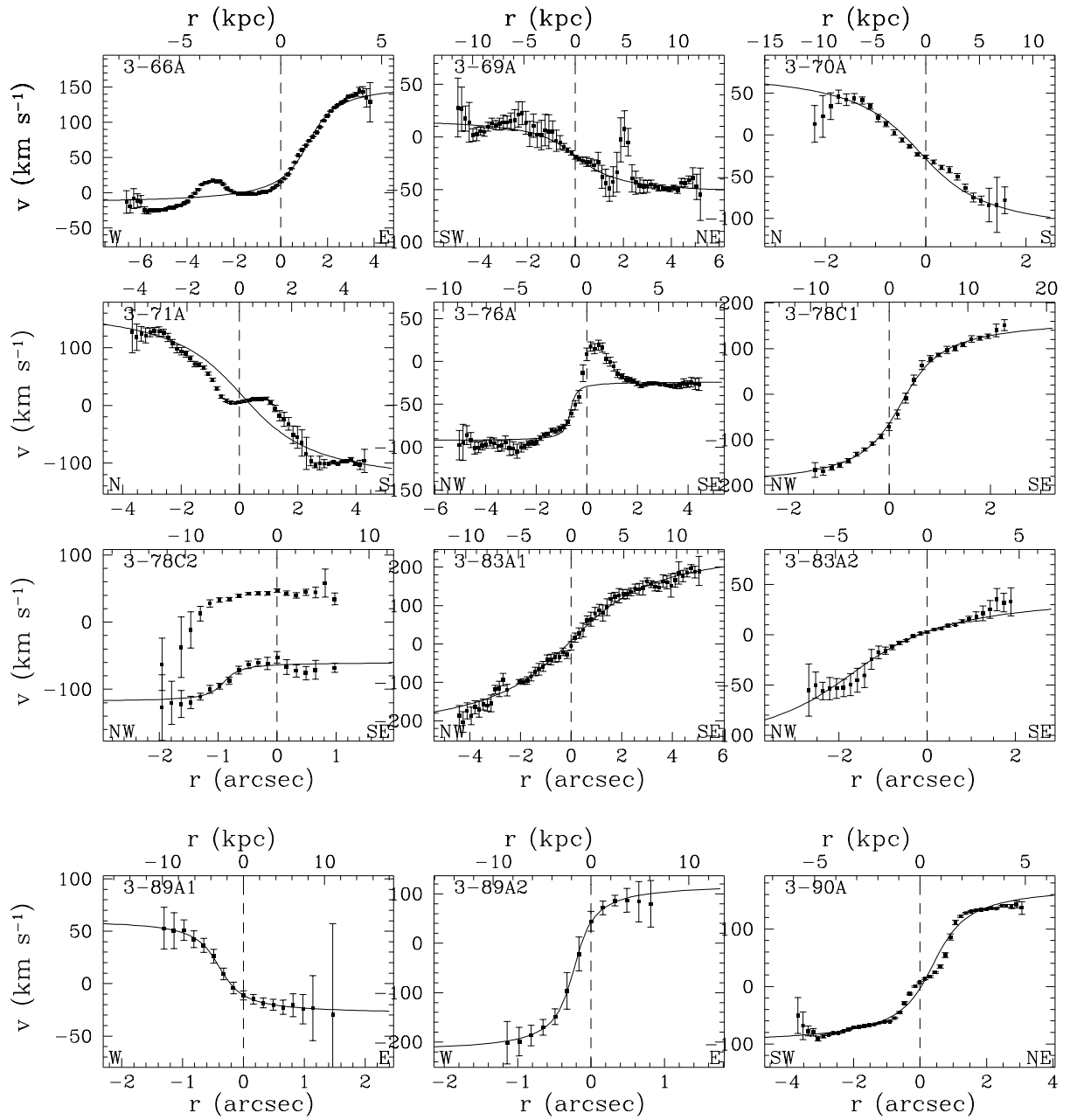


Fig. 10. The observed rotation curves for galaxies in our sample (at a mean $z \sim 0.1$). The solid line shows the fit with equation (3).

Table 3. Fluxes of the principal emission lines: red spectral region

Object	[SII] 6731	[SII] 6717	[NII] 6583	H α 6562	[NII] 6548	[OI] 6300	[OIII] 5007	[OIII] 4959	A_v mag
3-04A1	0.810±0.477	0.345±0.189	2.436±0.366	4.114±0.311	1.192±0.355	—	—	—	3.660
3-04A2	1.270±0.178	—	0.735±0.211	4.196±0.333	—	—	—	—	—
3-10A1	2.950±0.242	3.92 ±0.209	9.409±0.286	20.497±0.184	3.138±0.194	0.779±0.142	2.123±0.116	0.774±0.234	3.462
3-10A2	1.197±0.084	1.823±0.34	3.466±0.144	8.137±0.182	1.084±0.114	0.568±0.066	0.706±0.078	—	9.534
3-11A	—	—	49.68±12.0	14.93±6.0	—	—	—	—	—
3-12A	1.037±0.059	1.475±0.052	4.413±0.153	11.224±0.078	1.361±0.1	0.17 ±0.025	0.302±0.047	0.097±0.025	9.247
3-14A	0.705±0.31	0.54 ±0.225	2.537±0.353	6.686±0.428	—	—	—	—	—
3-16A*	0.052±0.011	0.080±0.018	0.292±0.022	0.429±0.021	—	—	0.026±0.008	—	9.241
3-17B	1.351±0.46	0.5 ±0.214	2.352±0.182	3.925±0.182	0.8 ±0.139	—	—	—	—
3-20A	0.80±0.072	1.083±0.067	0.706±0.135	4.069±0.077	0.218±0.034	0.247±0.039	2.904±0.200	1.034±0.034	0.911
3-21A	3.102±0.289	—	1.687±0.289	7.963±0.322	—	—	1.298±0.500	—	2.834
3-23A	—	—	0.919±0.122	2.169±0.133	0.259±0.108	—	—	—	—
3-24A	1.012±0.106	1.254±0.067	4.103±0.138	8.678±0.234	1.359±0.106	—	0.451±0.045	—	8.935
3-26A*	0.415±0.035	0.567±0.034	0.942±0.037	2.348±0.037	0.294±0.024	0.299±0.063	0.268±0.030	—	6.519
3-26B*	0.192±0.021	0.241±0.020	0.519±0.025	1.368±0.019	0.159±0.021	—	0.317±0.015	0.103±0.026	1.882
3-27A	1.94±0.105	2.27 ±0.133	6.030±0.169	12.378±0.184	1.928±0.202	0.605±0.13	1.581±0.175	—	8.700
3-27B	—	—	0.580±0.174	1.619±0.151	—	—	—	—	—
3-29A	0.467±0.092	0.596±0.076	2.111±0.08	1.833±0.276	0.72 ±0.089	—	0.154±0.071	—	9.741
3-30A	0.251±0.028	0.306±0.022	0.699±0.023	1.408±0.01	0.247±0.019	—	0.216±0.011	0.078±0.058	7.636
3-31A	—	—	1.489±0.988	6.014±0.064	—	—	—	—	—
3-36A*	0.277±0.074	0.396±0.026	0.928±0.070	2.042±0.149	0.301±0.044	—	0.089±0.026	—	7.942
3-36B	—	—	—	3.722±0.366	—	—	—	—	—
3-37A	2.879±0.155	3.443±0.236	12.769±0.374	18.56±0.836	2.89 ±0.141	0.721±0.113	0.764±0.158	—	8.773
3-38A	—	—	1.760±0.278	4.669±0.278	—	—	—	—	—
3-38B	8.186±0.932	—	5.510±0.577	9.883±0.377	—	—	—	—	8.322
3-39A1	—	—	0.941±0.079	2.494±0.11	0.306±0.047	—	—	—	8.577
3-40A	0.808±0.177	1.254±0.236	3.980±0.543	6.568±0.348	1.764±0.189	1.386±0.283	—	—	—
3-42A	2.167±0.200	—	2.936±0.2	4.347±0.167	1.12 ±0.211	0.539±0.099	1.216±0.160	0.265±0.120	2.920
3-44A1	3.172±5.290	—	4.150±0.238	1.956±0.224	2.193±0.426	—	2.473±0.277	1.004±0.410	—
3-44A2	0.143±0.06	0.332±0.046	0.500±0.114	1.606±0.143	0.164±0.074	—	0.085±0.049	0.264±0.084	9.151
3-45A*	0.211±0.033	0.287±0.032	0.646±0.031	1.327±0.026	0.196±0.026	0.091±0.031	—	—	8.919
3-47A	—	—	0.771±0.167	2.895±0.155	—	—	—	—	—
3-49A1	—	—	1.703±0.222	3.453±0.222	0.503±0.109	—	1.587±0.090	0.461±0.070	12.633
3-51A	0.834±0.411	0.282±0.133	—	4.527±0.289	—	—	—	—	—
3-53A1	0.779±0.051	0.932±0.044	1.653±0.064	4.501±0.254	0.398±0.037	0.537±0.099	0.913±0.084	0.472±0.088	9.672
3-54A1	3.556±1.443	3.158±0.888	3.813±0.389	21.778±0.366	—	0.904±0.2	5.377±0.380	2.015±0.400	2.724
3-55A	8.370±5.161	—	4.836±0.455	17.283±0.344	—	—	1.217±0.400	—	4.220
3-56A	—	—	0.640±0.366	2.317±0.455	—	—	—	—	—
3-57A1	2.436±0.133	2.983±0.1	4.049±0.91	8.880±1.554	1.338±0.444	0.983±0.244	1.137±0.250	—	14.044
3-58A	—	—	1.626±0.487	4.0410±0.418	0.51 ±0.371	—	—	—	—
3-59A	4.043±0.133	—	4.052±0.244	9.315±0.266	0.737±0.233	—	—	—	11.306
3-61A	1.331±0.488	1.694±0.3	3.773±0.466	8.116±0.511	—	—	—	—	—
3-64A	11.037±0.800	—	4.094±0.777	26.196±1.021	—	—	—	—	—

Table 3. continued

Object	[SII] 6731	[SII] 6717	[NII] 6583	H α 6562	[NII] 6548	[OI] 6300	[OIII] 5007	[OIII] 4959	A_v mag
3-65A1	2.543±0.059	3.371±0.076	8.507±0.446	22.833±0.209	2.234±0.446	0.431±0.047	1.333±0.154	0.378±0.034	7.702
3-65A2	0.854±0.044	1.148±0.103	1.522±0.276	5.308±0.324	—	0.346±0.047	0.585±0.036	0.147±0.023	9.654
3-66A	1.119±0.038	1.624±0.058	1.678±0.077	8.994±0.09	0.544±0.076	0.281±0.077	3.541±0.066	1.224±0.075	2.247
3-69A*	0.172±0.009	0.197±0.014	0.819±0.026	1.391±0.092	0.271±0.025	0.025±0.016	0.072±0.026	-	5.912
3-70A	0.467±0.018	0.566±0.068	3.037±0.024	2.524±0.109	0.881±0.021	0.185±0.015	4.186±0.160	1.468±0.181	4.481
3-71A*	0.695±0.057	0.842±0.058	2.230±0.118	5.545±0.110	0.657±0.041	0.124±0.034	1.222±0.147	0.537±0.135	13.073
3-73A	—	—	3.097±0.666	6.593±0.955	0.619±0.566	—	—	—	—
3-75A	0.109±0.078	0.193±0.041	0.366±0.061	0.723±0.058	0.092±0.056	—	—	—	—
3-76A*	0.150±0.034	0.182±0.026	0.478±0.053	1.172±0.053	0.155±0.022	—	—	—	7.257
3-77A	0.808±0.466	0.958±0.477	1.524±0.155	3.629±0.333	0.491±0.721	—	—	—	—
3-78A	—	—	0.719±0.144	2.298±0.155	—	—	—	—	—
3-78B	3.064±0.220		1.871±0.133	6.219±0.167	0.575±0.178	—	—	—	4.394
3-78C1	0.135±0.009	0.175±0.025	0.383±0.027	1.067±0.034	0.144±0.018	—	0.114±0.011	0.039±0.015	6.917
3-78C2	0.137±0.027	0.181±0.018	0.385±0.045	1.069±0.038	0.127±0.024	—	0.115±0.013	0.039±0.015	6.922
3-79A	4.913±1.332	7.027±1.221	19.86±0.966	41.248±0.844	5.843±1.11	0.472±0.322	—	—	4.465
3-79C	3.213±0.300		5.017±0.311	9.105±0.377	1.616±0.4	—	2.378±0.390	0.482±0.320	4.102
3-81A	—	—	8.790±0.844	23.843±1.11	—	—	—	—	—
3-81B	106.016±6.438		127.317±4.551	530.025±5.772	35.92±7.77	5.289±3.885	182.40±9.700	—	—
3-83A1	0.071±0.014	0.093±0.021	0.126±0.027	0.352±0.058	—	—	0.056±0.028	—	5.625
3-83A2	0.417±0.013	0.549±0.018	1.102±0.034	5.141±0.133	0.378±0.029	0.066±0.012	0.880±0.021	0.322±0.024	5.574
3-84A1	4.548±0.433	2.7 ±0.255	5.498±0.133	15.54±0.108	1.679±0.107	1.618±0.092	8.684±0.150	2.759±0.130	5.266
3-85A1	—	—	1.282±0.266	1.726±0.189	—	—	—	—	5.920
3-88A1	4.509±1.332	7.087±1.01	2.808±0.644	51.204±0.699	—	1.815±0.3	55.480±1.000	16.500±0.950	1.151
3-89A1	0.516±0.034	0.781±0.045	0.985±0.039	4.794±0.223	0.3 ±0.038	0.143±0.049	1.208±0.219	0.465±0.034	6.393
3-89A2	0.298±0.087	0.479±0.099	1.061±0.115	2.284±0.107	0.347±0.078	—	—	—	—
3-90A	0.457±0.043	0.509±0.038	1.413±0.051	3.407±0.061	0.456±0.036	0.041±0.016	0.128±0.040	—	7.283
3-91A	6.160±0.488		3.849±0.344	18.071±0.333	—	—	3.696±0.430	1.114±0.370	3.437
3-92A	1.487±0.111	2.03 ±0.093	2.415±0.311	13.353±0.322	—	0.768±0.133	3.258±0.350	1.047±0.220	8.252
3-92C	4.359±0.455		2.922±0.4	12.321±0.333	—	—	4.230±0.200	1.526±0.290	7.613
3-93A	3.746±0.266		1.952±0.2	9.398±0.189	—	0.199±0.133	2.220±0.320	0.966±0.340	3.654
3-96A	0.266±0.029	0.232±0.026	1.045±0.019	0.748±0.027	0.303±0.016	0.145±0.015	2.397±0.042	0.884±0.043	5.359

The fluxes, in unit of 10^{-18} erg s $^{-1}$ cm $^{-2}$ Å $^{-1}$, are not corrected for internal absorption. For H α we report here only the narrow component. The fluxes of the [SII] doublet are given separately, if available, otherwise the total flux of the doublet is given in the middle of the columns of the single lines.

Table 4. Fluxes of the principal emission lines: blue spectral region

Object	H_{β}	H_{γ}	[OII]	[OII]
	4861	4340	3729	3726
3-04A1	0.953±0.104	—	—	—
3-04A2	—	—	—	—
3-10A1	4.854±0.113	1.756±0.087	7.278±1.357	
3-10A2	0.973±0.156	0.246±0.046	0.849±0.328	0.769±0.265
3-11A	—	—	—	—
3-12A	1.386±0.126	0.414±0.028	0.557±0.138	0.705±0.318
3-14A	—	—	—	—
3-16A*	0.053±0.021	—	—	—
3-17B	—	—	—	—
3-20A	1.284±0.051	0.656±0.033	3.477±0.191	2.362±0.191
3-21A	2.024±0.364	—	—	—
3-23A	—	—	—	—
3-24A	1.11 ±0.155	0.229±0.059	1.592±0.857	
3-26A*	0.394±0.051	0.082±0.021	0.863±0.191	
3-26B*	0.387±0.110	0.08±0.015	—	—
3-27A	1.625±0.101	0.519±0.058	1.987±0.574	
3-27B	—	—	—	—
3-29A	0.214±0.105	—	—	—
3-30A	0.208±0.076	0.069±0.013	0.702±0.077	
3-31A	—	—	—	—
3-36A*	0.292±0.032	0.085±0.037	—	—
3-36B	—	—	—	—
3-37A	2.417±0.737	0.969±0.258	—	—
3-38A	—	—	—	—
3-38B	1.354±0.322	—	—	—
3-39A1	0.333±0.097	—	—	—
3-40A	—	—	—	—
3-42A	1.094±0.156	—	—	—
3-44A1	—	—	—	—
3-44A2	0.2 ±0.036	0.047±0.031	0.234±0.064	0.105±0.050
3-45A*	0.170 ±0.046	—	—	—
3-47A	—	—	—	—
3-49A1	0.291±0.076	—	—	—
3-51A	—	—	—	—
3-53A1	0.53 ±0.019	0.152±0.017	1.851±0.024	
3-54A1	5.604±0.499	—	—	—
3-55A	3.758±0.51	—	—	—
3-56A	—	—	—	—
3-57A1	0.64 ±0.218	—	—	—
3-58A	—	—	—	—
3-59A	0.912±0.302	—	—	—
3-61A	—	—	—	—
3-64A	—	—	—	—
3-65A1	3.354±0.049	1.128±0.044	2.361±0.095	2.865±0.092
3-65A2	0.626±0.072	0.160±0.01	0.450±0.088	0.779±0.127
3-66A	2.442±0.066	0.523±0.106	—	—
3-69A*	0.250±0.055	0.120±0.072	—	—
3-70A	0.533±0.035	0.158±0.022	0.396±0.024	0.296±0.027
3-71A*	0.445±0.087	0.072±0.024	—	—
3-73A	—	—	—	—
3-75A	—	—	—	—
3-76A*	0.181±0.054	—	—	—
3-77A	—	—	—	—
3-78A	—	—	—	—
3-78B	1.326±0.229	—	—	—
3-78C1	0.171±0.015	0.063±0.014	0.287±0.020	
3-78C2	0.17 ±0.017	0.063±0.019	0.290±0.024	
3-79A	8.725±0.77	—	—	—
3-79C	2.006±0.25	—	—	—
3-81A	—	—	—	—

Table 4. continued

Object	H $_{\beta}$ 4861	H $_{\gamma}$ 4340	[OII] 3729	[OII] 3726
3-81B	—	—	—	—
3-83A1	0.065±0.03	—	—	—
3-83A2	0.96 ±0.035	0.258±0.017	0.849±0.049	0.606±0.057
3-84A1	3.017±0.135	—	—	—
3-85A1	0.31 ±0.125	—	—	—
3-88A1	14.373±1.04	—	—	—
3-89A1	0.816±0.204	0.232±0.049	0.864±0.061	0.716±0.084
3-89A2	—	—	—	—
3-90A	0.525±0.031	—	—	—
3-91A	4.291±0.312	—	—	—
3-92A	1.844±0.302	—	—	—
3-92C	1.828±0.218	—	—	—
3-93A	2.178±0.291	—	—	—
3-96A	0.143±0.01	0.032±0.014	0.508±0.024	

The fluxes are in unit of 10^{-18} erg s $^{-1}$ cm $^{-2}$ Å $^{-1}$. The fluxes of the [OII] doublet are given separately, if available, otherwise the total flux of the doublet is given in the middle of the columns of the single lines.

Table 5. Spectral classification

Name	Class.	Name	Class.	Name	Class.
3-10A1	SF	3-42A	L	3-78C1	SF
3-10A2	SF	3-44A1	Sy	3-78C2	SF
3-12A	SF	3-44A2	SF	3-79C	SF
3-16A	SF	3-49A1	L	3-83A1	SF
3-20A	L	3-53A1	L	3-83A2	SF
3-21A	SF	3-54A1	SF	3-84A1	L
3-24A	SF	3-55A	SF	3-88A1	SF
3-26A	L	3-57A1	L	3-89A1	SF
3-26B	SF	3-65A1	SF	3-90A	SF
3-27A	SF	3-65A2	SF	3-91A	SF
3-29A	L	3-66A	SF	3-92A	SF
3-30A	SF	3-69A	SF	3-92C	L
3-36A	SF	3-70A	Sy	3-93A	SF
3-37A	SF	3-71A	SF	3-96A	Sy

Table 6. Kinematical parameters and masses.

Name	z	i [$^{\circ}$]	δ [$^{\circ}$]	r_{opt} [$''$]	R_{opt} [Kpc]	v_{opt} [km/s]	v_c [km/s]	Mass [$\log M_{\odot}$]	r_t [$''$]
3-10A1	0.0875	48	22	5.99	9.79	100	133	11.65	0.6
3-10A2	0.0867	38	74	2.99	4.50	50	271	11.92	0.4
3-12A	0.0775	24	14	5.97	8.74	25	58	10.89	—
3-16A	0.1176	51	6	3.31	7.33	117	140	11.57	1.8
3-20A	0.0736	71	15	6.78	9.43	90	92	11.31	—
3-23A*	0.0877	66	37	1.38	2.26	30	38	9.91	—
3-24A	0.1164	26	12	3.13	6.59	110	230	11.95	0.4
3-26A	0.0894	35	13	4.88	8.12	145	238	12.07	0.8
3-26B	0.0889	73	4	9.50	15.75	170	164	12.03	7.5
3-27A	0.0876	52	39	6.87	11.24	100	150	11.81	3.8
3-29A	0.0408	61	24	3.21	2.58	117	141	11.11	1.5
3-30A	0.2545	51	12	2.05	8.12	59	62	10.89	0.2
3-31A*	0.0267	37	5	16.50	8.79	50	81	11.17	—
3-36A	0.1183	69	0	3.01	6.43	145	139	11.50	0.4
3-37A	0.0507	43	16	3.06	3.02	30	44	10.16	0.4
3-38A*	0.0883	40	25	2.75	4.53	45	71	10.76	—
3-40A	0.0892	67	11	2.39	3.82	120	123	11.16	0.8
3-44A2	0.3027	52	58	1.44	6.46	95	175	11.70	0.5
3-45A	0.0791	64	2	4.28	6.39	176	182	11.73	1.3
3-47A*	0.0874	68	42	1.38	2.25	228	304	11.72	—
3-53A1	0.3723	22	25	0.74	3.80	36	77	10.76	0.1
3-59A*	0.0865	34	28	5.23	8.47	160	298	12.28	—
3-61A*	0.0545	50	47	6.33	6.69	306	555	12.72	—
3-65A1	0.1667	39	33	2.00	5.70	32	52	10.59	0.4
3-65A2	0.1672	33	88	2.47	6.49	11	—	—	0.1
3-66A	0.0536	62	5	7.50	7.80	90	97	11.27	0.9
3-69A	0.1043	47	2	5.21	9.96	29	36	10.51	1.3
3-70A	0.1970	17	78	1.65	5.38	80	—	—	—
3-71A	0.0516	42	8	4.28	4.29	110	161	11.45	—
3-76A	0.0800	33	58	5.05	7.61	35	112	11.39	0.2
3-78C1	0.2610	69	19	2.04	8.23	153	138	11.60	0.6
3-78C2	0.2611	83	50	1.76	7.10	25	31	10.24	0.2
3-81A*	0.0282	42	74	4.95	2.78	45	237	11.60	—
3-81B*	0.0264	85	30	1.00	0.56	90	102	10.17	—
3-83A1	0.1071	61	5	4.70	9.20	190	197	11.96	2.4
3-83A2	0.1071	35	12	2.85	5.78	55	89	10.06	1.7
3-88A1*	0.0516	67	32	2.48	2.46	180	219	11.48	—
3-89A1	0.2996	33	52	1.54	6.84	39	90	11.14	0.3
3-89A2	0.2992	46	0	1.00	4.45	160	171	11.52	0.2
3-90A	0.0721	42	15	4.10	5.62	118	170	11.62	0.8
3-93A*	0.0691	74	10	4.40	5.80	16	16	9.57	—

Columns: (1) galaxy name, (2) redshift, (3) galaxy inclination, (4) misalignment angle, (5) and (6) maximum radius of the rotation curve in arcsec and Kpc, respectively, (7) rotation velocity measured at R_{opt} , (8) mass derived by equation (1), (9) circular velocity, i.e., rotation velocity accounting for inclination and misalignment corrections (10) transition radius between the rising and flat parts of the rotation curve; * galaxies with TNG spectra.